

# Data-science-based reconstruction of 3-D membrane pore structure using a single 2-D micrograph

Hooman Chamani<sup>1</sup>, Arash Rabbani<sup>2</sup>, Kaitlyn P. Russell<sup>3</sup>, Andrew L. Zydny<sup>3</sup>, Enrique D. Gomez<sup>3,4</sup>, Jason Hattrick-Simpers<sup>5\*</sup>, Jay R. Werber<sup>1\*</sup>

<sup>1</sup>*Department of Chemical Engineering & Applied Chemistry, University of Toronto, Ontario M5S 3E5, Canada.*

*<sup>2</sup>School of Computing, University of Leeds, Leeds LS2 9JT, UK.*

<sup>3</sup>Department of Chemical Engineering, The Pennsylvania State University, Pennsylvania 16802, USA.

<sup>4</sup>*Department of Materials Science & Engineering, The Pennsylvania State University, Pennsylvania 16802, USA.*

<sup>5</sup>*Department of Materials Science & Engineering, University of Toronto, Ontario M5S 3E4, Canada.*

\*Corresponding authors:

J. Hattrick-Simpers

E-mail: jason.hattrick.simpers@utoronto.ca, Tel.: +1-416-978-3012.

J. Werber

E-mail: jay.werber@utoronto.ca, Tel.: +1-416-978-4906.

## Abstract

27 Conventional 2-D scanning electron microscopy (SEM) is commonly used to rapidly and  
28 qualitatively evaluate membrane pore structure. Quantitative 2-D analyses of pore sizes can be  
29 extracted from SEM, but without information about 3-D spatial arrangement and connectivity,  
30 which are crucial to the understanding of membrane pore structure. Meanwhile, experimental 3-D  
31 reconstruction via tomography is complex, expensive, and not easily accessible. Here, we employ  
32 data science tools to demonstrate a proof-of-principle reconstruction of the 3-D structure of a  
33 membrane using a single 2-D image pulled from a 3-D tomographic data set. The reconstructed and

34 experimental 3-D structures were then directly compared, with important properties such as mean  
35 pore radius, mean throat radius, coordination number and tortuosity differing by less than 15%. The  
36 developed algorithm will dramatically improve the ability of the membrane community to  
37 characterize membranes, accelerating the design and synthesis of membranes with desired structural  
38 and transport properties.

39

40 **Keywords:** Data science; 3-D reconstruction; Membrane microstructure; Electron microscopy; Pore  
41 analysis.

42

43 **1. Introduction**

44 Porous membranes are vital in advanced fields like catalysis, biopharmaceutical separations,  
45 batteries, biosensing, microfluidics, air filtration, and water treatment [1]. Porous membranes are  
46 thin layers (typically < 100  $\mu\text{m}$ ) in which the pores are engineered such that the membrane has high  
47 flux and selectivity, while tolerating the required range of operating pressures and temperatures.  
48 Characterization of porous membranes in terms of key structural parameters, such as pore size  
49 distribution (PSD) and throat size distribution (TSD), is imperative to fundamentally understand  
50 structure/transport/performance relationships [2]. For instance, knowing PSD and TSD permits the  
51 evaluation of how particle retention takes place in membranes used for separation processes, as the  
52 throat and small pores are the locations where particles are captured.

53 Different physical techniques have been presented for estimation of pore size and PSD including  
54 gas-liquid porometry, liquid-liquid porometry, liquid-vapor equilibrium method, gas-liquid  
55 equilibrium method (permoporometry), liquid-solid equilibrium method (thermoporometry), and  
56 mercury porosimetry. Among these methods, the gas-liquid and liquid-liquid porometry techniques

57 have been most frequently employed [3]. In these approaches, the membrane is wetted with a liquid,  
58 which is then displaced using gas for membranes with large pores ( $> 500$ -nm diameter) or an  
59 immiscible liquid with low surface tension for membranes with smaller pores (as small as 2-nm  
60 diameter). The obtained flow rate vs. applied pressure curves are then used for the estimation of  
61 PSD. Although these methods are quick, reproducible, and affordable, they have drawbacks,  
62 including error associated with uncertainties in the contact angle [3–6], assumption of circular  
63 cylinders [3], and the possibility of membrane compression during testing. More crucially, these  
64 methods require modeling membranes as an array of discrete, parallel pores, which does not suitably  
65 capture the anisotropic, complex, and highly connected nature of real membranes.

66 Scanning electron microscopy (SEM) and transmission electron microscopy (TEM) are methods  
67 used frequently to qualitatively characterize the pore size, pore shape, morphology, and structure of  
68 membranes [2,7–10]. SEM is used routinely, both for analysis of membrane surface pores and for  
69 analysis of membrane cross-sections to assess the overall pore structure. However, quantitative  
70 analysis of electron micrographs is uncommon and typically limited to 2-D images, which can yield  
71 properties such as surface PSD, surface porosity, overall porosity, total membrane thickness, and  
72 selective layer thickness, but cannot directly yield information about the actual 3-D PSDs, tortuosity,  
73 spatial pore arrangement, and connectivity of pores. Quantitative analysis of surface pores from top-  
74 view 2-D images requires the assumption that the minimum pore size occurs directly at the upper  
75 surface, which is insufficient for complete modeling and not true in many cases [2]. The limitations  
76 of analyzing membranes using 2-D images typically necessitates reconstructing the 3-D structure of  
77 the membrane for comprehensive analysis.

78 Serial sectioning is a proven experimental technique for obtaining 3-D information from methods  
79 that conventionally produce 2-D data. The technique is composed of two primary steps, (i)

80 iteratively sectioning a material at desired depth increments and (ii) collecting data from each  
81 section. Sectioning can be done by several different methods, including polishing, cutting, laser  
82 ablation, grinding, and ion sputtering [11]. Sectioning and imaging are repeated until the required  
83 material volume is interrogated. Following the completion of the experimental data collection, 3-D  
84 structures are rebuilt and examined through image-processing and visualization programs. Serial  
85 sectioning tomography experiments may now be scaled down to analyze features at the nanometer  
86 scale because of the development of focused ion beam (FIB) and FIB-SEM instruments [12]. Other  
87 techniques for 3-D pore visualization, particularly X-ray computed tomography, have been used for  
88 3-D membrane reconstruction [13,14]; however, given that X-ray computed tomography is limited  
89 to resolutions typically  $> 1 \mu\text{m}$ , FIB-SEM is preferred over other techniques for membrane  
90 characterization owing to its resolution approaching 1 nm [15].

91 In membrane science, FIB-SEM has recently enabled comprehensive analysis of  
92 structure/performance relationships. The technique has been employed to examine microfiltration  
93 [16,17], ultrafiltration [18], reverse osmosis [19], and viral filtration membranes [20]. In these  
94 studies, 3-D reconstructions of membrane structure were typically obtained with a resolution of 3–5  
95 nm, allowing for calculation of porosity, average pore size, distribution of pores and throat sizes,  
96 and percentage of dead-end pores. Also, it made it possible to see how pores in various membrane  
97 regions were connected to one another. Critically, fluid flow in the obtained 3-D pore structures can  
98 be simulated using computational fluid dynamics (CFD), enabling insight into performance metrics  
99 such as the deposition of particles [20], water permeability [20], and air flow rate [21].

100 Despite its clear benefits, generating 3-D tomographic images from FIB-SEM remains challenging  
101 for soft, poorly conducting materials such as polymeric membranes, which are sensitive to ion and  
102 electron beam damage. Typical challenges include charging, cross-sectioning artifacts, and

shadowing impacts, which take place when surrounding materials shadow a pore [22]. In addition, FIB-SEM is expensive, requires months of optimization, and is not easily accessible, leading to just nine studies that we are aware of on membrane 3-D reconstructions using FIB-SEM [16–20,23–26]. The time-consuming nature of FIB-SEM also limits sample volumes, which are typically on the order of 1–10  $\mu\text{m}^3$  and can only focus on a small part of the membrane (e.g., the region near the membrane inlet or outlet).

Given the rapid innovation in membrane science occurring to address sustainability and technological challenges, there is a clear need for an accessible and rapid method for generating representative 3-D pore structures. Reconstructing the membrane 3-D pore structures using a few 2-D cross-sectional SEM images has the potential to address and fulfil this demand. For example, in a recent study, the 3-D asymmetric structures of block-copolymer-based ultrafiltration membranes were simulated by generating a stochastic pore network model from 2-D SEM images [27]. The model enabled rapid estimation of water permeability, which reasonably agreed with experimental water permeabilities. However, the simplified 3-D pore network model was not validated against an experimental 3-D structure, as a suitable 3-D structure was not available.

In this study, we use data science to create statistically representative 3-D membrane structures using single 2-D images. To develop the algorithm, we used a recently published tomographic FIB-SEM data set [20] from an ultrafiltration membrane used for viral filtration, which enabled us to (i) pull individual 2-D cross-sectional SEM images as inputs to the algorithm and (ii) assess the validity of the algorithm by comparing the experimental and reconstructed 3-D structures. During the optimization of the digitally-created structure, the algorithm only considers a single 2-D input image, with statistical features of the input image compared with a 2-D slice of the digitally-created structure. The structural and performance properties of the obtained 3-D structure were then

126 compared with those calculated from the original reconstruction. With further optimization, the  
127 method could revolutionize the structural characterization of membranes, enabling rapid and  
128 inexpensive generation of rich 3-D-based data sets to accelerate membrane development.

129

130 **2. Materials and methods**

131 **2.1. Membrane FIB-SEM data set**

132 In a previous study [20], the combination of FIB and SEM (FIB-SEM) was used to obtain a 3-D  
133 reconstruction of a virus filter (Viresolve® Pro) from MilliporeSigma, in which a dual-beam FEI  
134 Helios 660 FIB-SEM was utilized for imaging. More details about the operational parameters  
135 including voltage, beam current, and tilt angle can be found in the literature [20]. After taking  
136 images, several steps were done to create 3-D structures of the membrane, namely tilt correction,  
137 image alignment, and grayscale adjustment for slice brightness variation (Fig. S1). The data set  
138 obtained from this study was used for model development in the current research. This data set was  
139 composed of the raw electron micrographs, containing 407 images (or slices) taken at 3-nm slice  
140 increments (Data S1). We neglected the last 7 slices owing to some defects found in the last slices.

141 **2.2. Membrane 3-D reconstruction**

142 The 3-D reconstruction algorithm was developed in the MATLAB environment (MathWorks) using  
143 the Computer Vision, and Statistics and Machine Learning Toolboxes. We repeated the  
144 reconstruction process five times, generating five 3-D structures. The confidence interval was  
145 calculated for the properties and performance parameters of the membrane. The confidence interval  
146 can be calculated by its margin of error. The interval margin of error is dependent on the confidence  
147 level that is chosen [28]. 95% interval is one of the most common choices that has been used in the

148 literature [29,30]. The margin of error for the 95% confidence interval is calculated as  $1.96 \times \frac{SD}{\sqrt{N}}$ ,  
149 where SD is the standard deviation and N is the sample size [28].

150 **2.3. Pore network model**

151 We used the Pore Network Modeling extension of Avizo software (Thermo Fisher Scientific) for  
152 spatial analysis. The 3-D structures were initially converted to the .tiff format and then imported to  
153 the Avizo environment, in which larger spheres were used to represent pore bodies connected by  
154 narrow cylinders, i.e. throats (throat refers to constrictions between pores, see Fig. S2). After  
155 thresholding, total porosity was calculated. Axis Connectivity module was then utilized to calculate  
156 the connected porosity. For separating pore pathways, we employed the Separate Objects module,  
157 which computes watershed lines on a distance map. The Generate Pore Network module was then  
158 utilized to calculate PSD, TSD, coordination number distribution, and tortuosity. This module made  
159 it possible to retrieve various statistics from a labelled and divided pore space.

160 **2.4. Permeability and rejection**

161 By employing the FlowDict module of GeoDict (Math2Market, Germany), the water flux through  
162 the 3-D structure was assessed by solving the Stokes flow equation at a pressure difference of 210  
163 kPa. Gold nanoparticles have been utilized in several studies to assess the pore size and retention  
164 properties of virus filters [31,32]. We used the FilterDict-Media solver to model gold nanoparticle  
165 retention under the same pressure as that used to calculate the permeability. At the membrane inlet,  
166 feed was supplemented with 20 nm nanoparticles (concentration of  $10^8$  particles/mL). Particle-  
167 particle and particle-wall collisions, along with Brownian diffusion, were all taken into  
168 consideration for nanoparticle transfer through the 3-D structures. When a nanoparticle's diameter is

169 equal to or greater than the pathway accounting for the 3-D structure of the pore space, nanoparticle  
170 capture would take place.

171

172 **3. Results and Discussion**

173 **3.1. Image segmentation**

174 To develop the algorithm, we used a published FIB-SEM data set (Data S1) of the Viresolve® Pro  
175 [20], a commercial membrane that is used in bioprocessing to remove putative viruses as small as 20  
176 nm in diameter from therapeutic proteins; this is typically classified as an ultrafiltration membrane.  
177 In this data set, there were 400 cross-sectional SEM images (slices) taken sequentially at 3-nm  
178 increments. We have oriented the data set such that the electron micrographs were imaged  
179 sequentially in the y-direction, with the z-axis describing depth through the membrane and the x-y  
180 plane at z=0 being the top surface (Fig. S5).

181 The algorithm starts by selecting a random slice and performing image segmentation, in which a  
182 label is assigned to each pixel of the image such that pixels with the same label have similar visual  
183 characteristics [33]. The easiest segmentation approach is thresholding [34]. When segmenting an  
184 image using the thresholding technique, any pixels whose intensity levels exceed the threshold are  
185 fixed to a foreground value; the other pixels will have a background value. Using this method, a  
186 grayscale image can be converted into a binary image [35]. In the previous study [20] in which FIB-  
187 SEM was used to reconstruct the 3-D structure of the membrane, a conventional thresholding  
188 method was employed in which a global threshold is applied to all pixels. As can be seen in Fig.  
189 S3B, the conventional thresholding method was not fully successful in identifying pore-solid  
190 boundaries. Here, we utilized adaptive thresholding, where the threshold value dynamically changes  
191 at different parts of the image. The adaptive thresholding algorithm in MATLAB [36] was used, in

192 which the local mean intensity around each pixel is used to determine the threshold value (Fig.  
193 S3C).

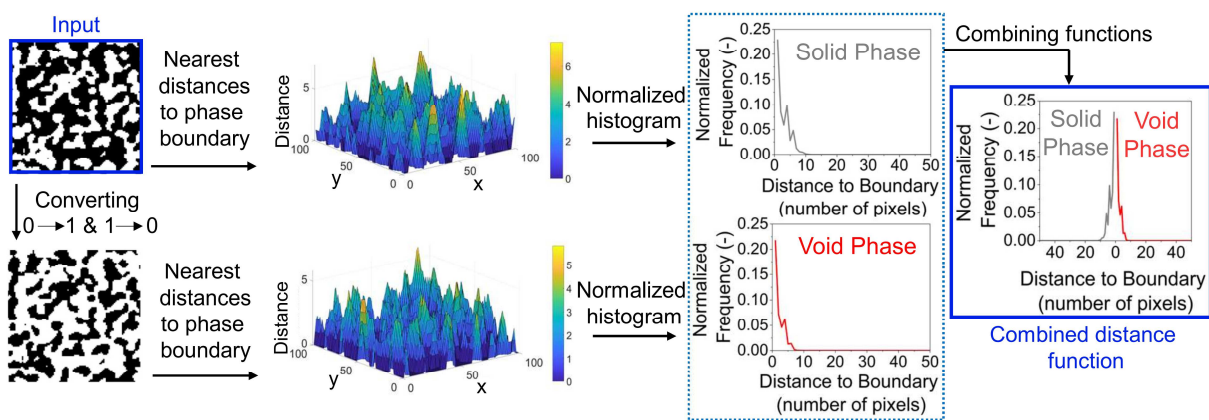
194 **3.2. Feature extraction from 2-D images**

195 In the computer-vision field, a “feature” is defined as a measurable piece of data that is extracted  
196 from the image. Working with features of the image, instead of the image, decreases information  
197 redundancy and reduces computational intensity during model training. A challenging topic in  
198 computer vision is to extract information-rich features that capture the intrinsic content of the  
199 images [37]. For instance, in this study, the segmented image selected from the FIB-SEM data has  
200  $899 \times 1024$  pixels, i.e., 920,576 elements. We reduced the number of elements from 920,576 to 100  
201 by using a histogram of the distance map as the feature. In a previous study, Rabbani et al. [38]  
202 calculated the Lattice Boltzmann Method-based absolute permeability of throats and compared the  
203 calculated permeabilities with various features extracted from images of porous structures (in this  
204 case porous rocks), including cross-sectional area, axes ratio, equivalent radius, solidity (area of the  
205 throat convex hull divided by the throat area), and mean distance map. It was observed that the  
206 averaged distance map of the throat was highly correlated with water flow [38], suggesting the  
207 usefulness of distance maps for analysis of porous structures. Distance maps have also been  
208 employed in other fields including prediction of thermal conductivity of woven ceramic composites  
209 [39], binarization of degraded document images [40], fingerprint matching [41], and tumor  
210 characterization [42].

211 Here, we employed a novel distance map to capture the statistical distribution of the pore and solid  
212 through a membrane. After image segmentation, 0s were assigned to void (pore) spaces and 1s were  
213 assigned to solid spaces. The Euclidean distance between each pixel and the nearest non-zero pixel  
214 was calculated (Fig. S4). Instead of the averaged distance map used by Rabbani et al. [38], we used

215 a normalized histogram of the distance map. Fig. 1 (top of the figure) illustrates the steps used to  
 216 develop a normalized histogram of the distance map for a synthetic binary image. Each histogram  
 217 was normalized to the total number of pixels in the image. To generate the normalized histogram of  
 218 the distance map for the void space, similar calculations as those used for the solid phase were  
 219 repeated (bottom of Fig. 1). Afterward, we combined the normalized histograms to yield a single  
 220 combined distance function (CDF) (Fig. 1).

221



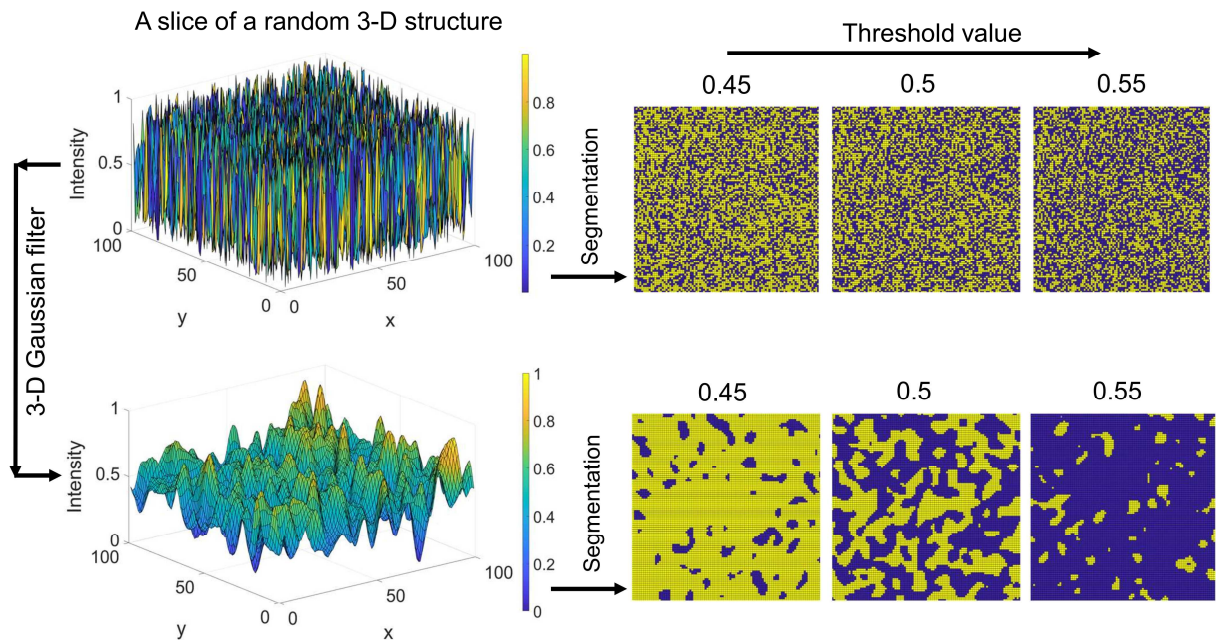
222  
 223 Fig. 1. Combined distance function for optimization of the membrane structure. For each 2-D  
 224 micrograph, the matrix of the nearest distance to the phase boundary (in other words, the distance  
 225 map) is calculated for both solid and void phases in the form of a histogram. These two histograms  
 226 are then combined to generate the combined distance function.

227

### 228 3.3. Generating 3-D structures

229 The next step is to enable rapid and optimizable *in silico* generation of 3-D porous structures.  
 230 Initially, a 3-D matrix ( $A_1$ ) with the same size as that of the original FIB-SEM structure  
 231 (1024×899×400 pixels) was generated to represent the membrane. The matrix elements were  
 232 randomly set to values between 0 and 1. To generate spatial correlation, we filtered  $A_1$  with a 3-D  
 233 Gaussian smoothing kernel (Fig. 2). The standard deviation of the Gaussian filter affects the pore  
 234 sizes. To account for depth-dependent anisotropy in pore size (i.e., a trend towards increasing pore

235 size with depth as one moves away from the membrane skin layer), a second matrix ( $A_2$ ) was  
 236 generated with the same dimensions as  $A_1$ . A second Gaussian filter was used with a larger standard  
 237 deviation to represent the larger pores occurring towards the bottom of the membrane. To vary pore  
 238 size with depth, we generated a new matrix ( $A_T$ ) by combining  $A_1$  and  $A_2$ , with relative proportions  
 239 of the two matrices weighted by the distance between each cell (or pixel) and the top of the 3-D  
 240 structure (Fig. S5).



241  
 242 Fig. 2. 3-D Gaussian filter and subsequent thresholding. The influence of the Gaussian filter on  
 243 the structure of a synthetic random micrograph with a sigma (standard deviation) of 2.  
 244

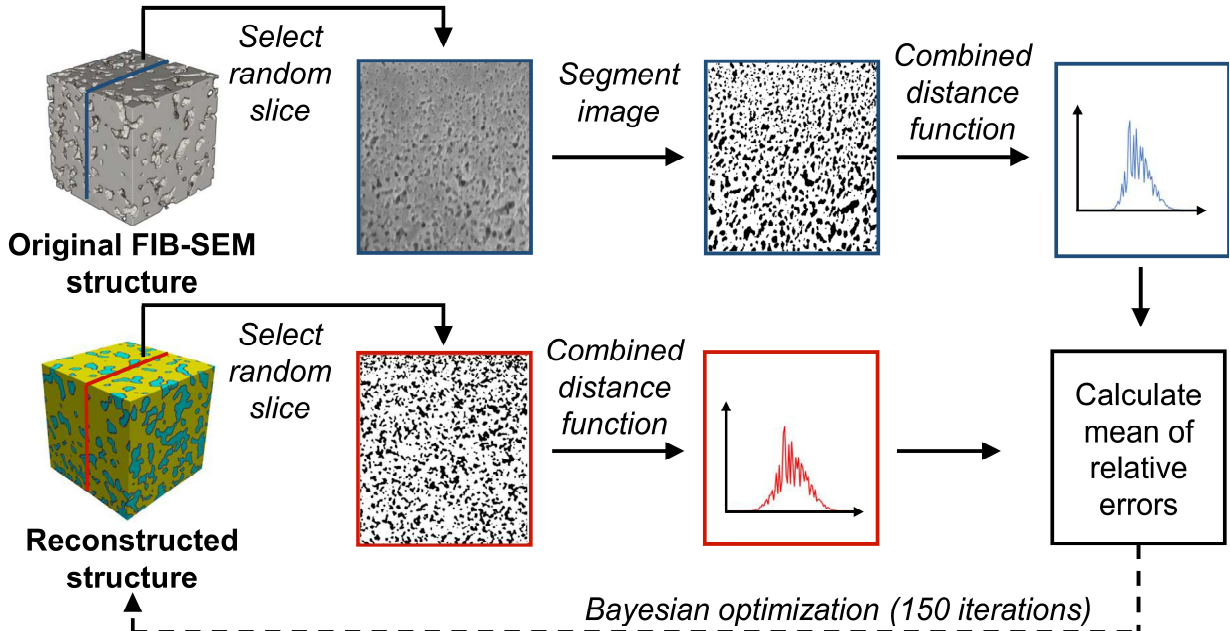
245 Since cells of  $A_T$  have values between 0 and 1, thresholding must then be applied on  $A_T$  using a cut-  
 246 off value to binarize the matrix and differentiate between void and solid phases. The cut-off value  
 247 for this round of thresholding is an important parameter during optimization (Fig. 2). In the next  
 248 step, morphological closing was used to smooth the sharp corners and make the pores more circular.  
 249 For this purpose, we used the *imclose* function of MATLAB to perform morphological closing using

250 a structuring element, which defines the pixel in the image being processed and the neighborhood  
251 used in the processing of each pixel. The radius of the structuring element controls the level of  
252 rounding of the pores; a larger radius in the structural element results in more circularity of the  
253 pores. The standard deviations of the Gaussian filters applied on  $A_1$  and  $A_2$ , the thresholding value  
254 after forming the weighted average  $A_T$ , and the radius of the structuring element during  
255 morphological closing are the four parameters that determine the final 3-D reconstructed structure.

256 **3.4. Optimization of 3-D structure**

257 To optimize the generated 3-D structure, the algorithm pulls a random cross-sectional slice from the  
258 3-D reconstructed structure (Fig. 3). The combined distance function of this slice can then be  
259 determined, and the cumulative absolute difference with the combined distance function of the input  
260 micrograph can be calculated. To account for morphological differences in the membrane skin layer  
261 (top region near the surface) and the underlying substructure, we divided each image into two  
262 sections, the top 20 percent with smaller pores and the bottom 50 percent with larger pores. For each  
263 section, a separate combined distance function was generated (Fig. S6). We did not include the  
264 middle 30 percent in the model because in this area there was a transition region from small to large  
265 pores, which complicated the optimization process.

266 Compared to other approaches of optimization, Bayesian optimization is a sample-efficient method  
267 to find superior solutions for finite and noisy data [43]. We used the BayesOpt library of MATLAB  
268 [44] to optimize the standard deviations of the Gaussian filter applied on  $A_1$  and  $A_2$ , the thresholding  
269 value, and the radius of the structuring element to minimize the cumulative error between the  
270 combined distance functions of slices of the 3-D reconstructed structure (for the top and bottom of  
271 the image) and the initial 2-D image selected from the original FIB-SEM data set (Fig. 3).



272  
 273 Fig. 3. Overview of the reconstruction algorithm. A single slice of the original FIB-SEM  
 274 is selected randomly, and after image segmentation, the combined distance function is generated.  
 275 The algorithm generates random 3-D reconstructed structures which are then optimized using  
 276 Bayesian optimization with the aim of minimizing the error between the combined distance functions of  
 277 a slice of the reconstructed structure and the one selected from the original FIB-SEM image.

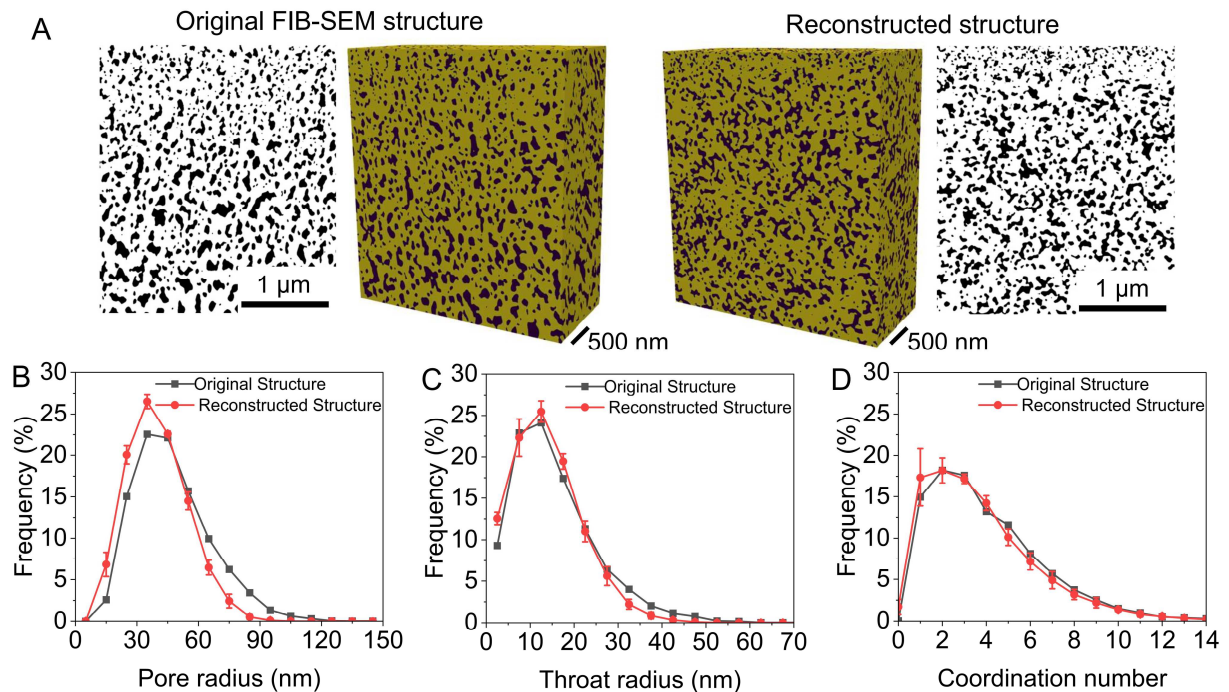
278  
 279 **3.5. Pore network model**

280 After optimization, a 3-D reconstructed structure is obtained for which a random 2-D slice has a  
 281 statistically similar morphology compared to the input micrograph according to the combined  
 282 distance function. Since the input micrograph corresponded to a 3-D FIB-SEM data set, we are also  
 283 able to extract and compare the properties of the 3-D structures (Fig. 4), allowing us to assess  
 284 whether optimization using the 2-D image results in statistically similar 3-D structures. The void  
 285 space in porous materials has previously been studied using pore-network models [45–48]. A  
 286 straightforward pore network model is presented to describe the void/solid phase as a collection of  
 287 bodies and throats (Fig. 5), with the aim of quantifying the membrane properties. Given that the  
 288 initial matrix construction was based on random numbers and the slice for comparison was selected

289 randomly, there are some sources of uncertainty in the model. We therefore repeated the model  
290 calculations five times.

291 We first compare the overall properties of the membranes, including the pore radius distribution,  
292 throat radius distribution, and coordination number distribution (Fig. 4B-D). The coordination  
293 number is the number of connected neighbors for a given pore. For instance, a coordination number  
294 of 0 means that the pore is isolated. All three distributions show remarkable similarities between the  
295 original and reconstructed structures. Each reconstructed structure is based on a single 2-D  
296 micrograph, while the original is based on 400 images, and therefore the agreement seen in Fig. 4B-  
297 D is surprising. Table 1 compares the reconstructed and original structures quantitatively. The mean  
298 body radius of the original structure is 47.1 nm, while the mean body radius of the reconstructed  
299 structures is  $40.0 \pm 1.4$  nm. The error bars refer to a 95 percent confidence interval for the expected  
300 mean.

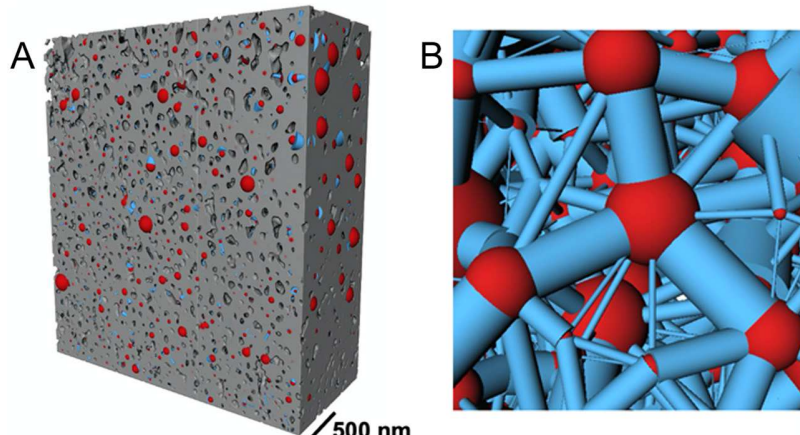
301



302

303 Fig. 4. Comparison of the original and reconstructed structures. (A) 2-D and 3-D comparison of the  
304 original FIB-SEM and reconstructed structures, and comparison of bulk properties, including (B)  
305 body radius distribution, (C) throat radius distribution, and (D) coordination number distribution for  
306 the entire structure studied, i.e., the 3  $\mu$ m depth beginning at the skin layer. 95% confidence interval  
307 is calculated for Fig. 4 B-D. Frequency is the ratio of the number of pores or throats in a particular  
308 bin to the total number of pores or throats.

309



310  
311 Fig. 5. Pore network model for the original 3-D structure generated using FIB-SEM. (A) Pore  
312 network model within the 3-D structure (the skin layer is located on the bottom side of this figure),  
313 and (B) pore network model with high magnification. This figure is a collection of pores and throats  
314 in which red displays bodies and blue illustrates throats. Analysis was done using Avizo.  
315

316 The trend of overall porosity—defined as the ratio of the pore volume to total volume—through the  
317 membrane was similar for both the original and reconstructed structures (Fig. S7), showing that the  
318 depth-dependent porosity has almost the same range for both structures. Another advantage of  
319 having the complete 3-D structure is that the portion of inaccessible pores—i.e., pore area that is  
320 completely disconnected from either the reconstruction's inlet and exit surfaces—can be calculated,  
321 whereas porometric methods can only assess pores that are connected to both the membrane inlet  
322 and exit. Both total and connected porosity are estimated for reconstructed structures with very low  
323 errors compared to the original structure. Tortuosity is another membrane parameter affecting mass  
324 transfer within the membrane. This parameter is typically described as the ratio between the actual  
325 distance traversed between two points and the distance traveled in a straight line connecting the  
326 same two points. Therefore, tortuosity can never be less than 1 [49]. The developed approach in this

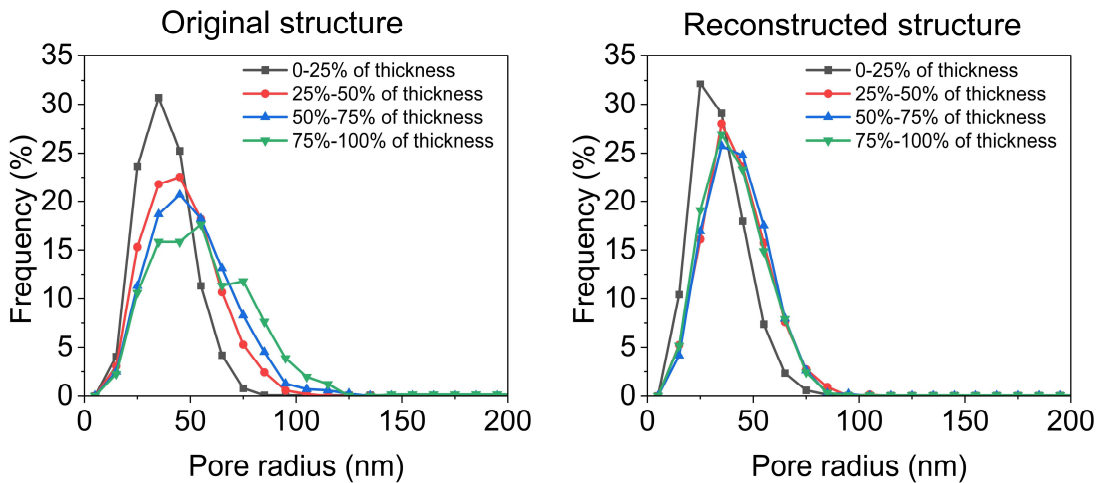
327 study allows us to calculate the tortuosity of the membrane using a single 2-D micrograph with very  
 328 high accuracy and low standard deviation (Table 1).

329  
 330 **Table 1. Comparison between original and reconstructed structures in terms of properties and**  
 331 **performance for the entire structure studied.**

	Mean body radius (nm)	Mean throat radius (nm)	Mean coordination number (-)	Porosity (total)	Porosity (connected)	Tortuosity	Permeability (LMH/psi)
<b>Original structure</b>	47.1	15.6	4.07	0.252	0.249	1.7	13.3
<b>Reconstructed structure #1</b>	39.3	13.3	3.62	0.251	0.241	1.76	6.5
<b>Reconstructed structure #2</b>	39.8	14.1	3.75	0.261	0.256	1.73	10.7
<b>Reconstructed structure #3</b>	37.7	12.6	3.29	0.248	0.236	1.77	5.2
<b>Reconstructed structure #4</b>	41.3	15.1	3.74	0.277	0.271	1.72	11.8
<b>Reconstructed structure #5</b>	42.1	14.3	4.62	0.276	0.274	1.72	14.3
<b>Average of reconstructions (with 95% confidence interval)</b>	40.0 ± 1.4	13.9 ± 0.8	3.80 ± 0.39	0.263 ± 0.011	0.256 ± 0.013	1.74 ± 0.02	9.7 ± 3.0
<b>Error (%)</b>	15	10	6.6	4.3	2.8	2.3	27

332  
 333  
 334 While the reconstructed and original structures have similar transport characteristics and overall  
 335 properties, the depth-dependent PSDs differ marginally (Fig. 6). The PSD continues to broaden  
 336 slightly with depth for the original structure, while for the reconstructed structure, there appears to

337 be two distinct layers. Future work will aim to improve the algorithm's capture of depth-dependent  
338 pore-size variability.



339  
340 Fig. 6. Depth-dependent pore size distribution. Pore size distribution through the depth of the  
341 membrane (in the flow direction, i.e. Z direction, see Fig. S5 for defining directions) for both  
342 original FIB-SEM and reconstructed structures, where 0-25% of thickness refers to the  
343 uppermost region of the membrane containing the skin layer. Frequency is the ratio of the  
344 number of pores in a particular bin to the total number of pores.  
345

### 346

### 347 **3.6. Simulations of water and particle transport**

348 Common transport models used for estimating fluid flow through membrane pores—namely the  
349 Hagen–Poiseuille equation, Washburn's equation, and Cantor's equation—assume that membranes  
350 comprise discrete cylindrical pores, which dramatically simplifies the highly complex and  
351 interconnected nature of true membrane structures. CFD simulations of transport through 3-D  
352 structures can provide fundamental insights of the impact of structure on transport—for example,  
353 enabling tracking of water velocity through the structure (Fig. S8). These simulations could also  
354 serve as validation for more involved mathematical models [27,50].

355 We used GeoDict to simulate the transport of water passing through the pores of the 3-D structure of  
356 the membrane via CFD simulations. GeoDict has previously been utilized for flow and particle

357 capture behavior in membrane science [20,51,52]. Since images were taken from the size-selective  
358 skin layer only to a depth of 3  $\mu\text{m}$ , the substructure of the membrane with larger pores were by  
359 necessity neglected. The substructure is anticipated to have a low contribution to the resistance to  
360 flow because of the fast-expanding pore size trend observed in the membrane structure [31]. It has  
361 already been shown that the original structure obtained from FIB-SEM is an excellent proxy of the  
362 real membrane [20]; here our goal is to compare simulated transport in the original FIB-SEM and  
363 reconstructed structures. As shown in Table 1, the average estimated water permeability for  
364 reconstructed structures is 9.7 LMH/psi, which is 27% lower than the original FIB-SEM structure.  
365 This error is greater than those for morphological properties, resulting from water permeability  
366 being highly sensitive to the structure of the membrane. For the same reason, the permeabilities of  
367 the reconstructed structures vary relatively substantially, with a coefficient of variation of 30%  
368 compared to 3.5% for the mean body radius. The variation in simulated water permeability is  
369 analogous to experimental permeability measurements using small coupons of the same membrane,  
370 for which multiple measurements must be done to determine a meaningful average.

371 Similar retention properties of gold nanoparticles as those of bacterial and mammalian viruses make  
372 them a good proxy for simulating the rejection of virus filters [20]. Simulation of the rejection  
373 process demonstrates that the reconstructed structures retain gold nanoparticles with 100%  
374 efficiency, with a log reduction value (LRV) greater than or equal to 2.7. The original FIB-SEM  
375 structure similarly displays 100% rejection, with a LRV greater than or equal to 2.9. The original  
376 and reconstructed structures thereby display highly similar rejection properties for 20-nm particles.

377

378 **4. Conclusion**

379 In this study, a novel approach was developed to reconstruct the 3-D structure of the membrane  
380 using only a single 2-D cross-sectional micrograph. Spatial knowledge of the 3-D internal pore  
381 structure enables comprehensive structural analysis and exact transport simulations, both of which  
382 are impossible when using conventional porometric techniques that only provide pore-size  
383 distributions based on a model of the membrane as having an array of parallel pores. Ideally,  
384 researchers would be able to do FIB-SEM on each of their samples to obtain these 3-D structures;  
385 however, this will never be possible given the complexities and cost of the technique. Our approach  
386 is a first step towards the routine characterization of 3-D internal pore structures during membrane  
387 development based on readily obtainable 2-D cross-sectional images through the depth of the  
388 membrane. A few key properties enabled the algorithm to successfully achieve our goal of rapidly  
389 creating statistically similar 3-D structures using a 2-D input. First, adaptive thresholding enabled  
390 robust and precise image segmentation, with the segmented images reflecting void and solid phases  
391 even in the presence of shadows (Fig. S3, Table S1). Second, the selected feature (i.e., combined  
392 distance function) was not only able to extract significant information embedded in the image—as  
393 demonstrated by the similar properties of the original and reconstructed membranes—but also  
394 proved to be similar for all slices of the FIB-SEM data set (Fig. S9). This repeatability suggests  
395 that—for this 3-D section of a membrane—selecting a random slice does not introduce meaningful  
396 uncertainty to the model, enabling a single micrograph to be used as the model input in this study. In  
397 the case of dealing with complex structures, where in addition to the vertical (fluid flow) direction,  
398 the homogeneity assumption does not hold in the lateral directions, the selected features will not be  
399 the same for all slices in lateral directions, and reconstruction based on a single image might result  
400 in an inaccurate microstructure. Future work will aim to develop methods to accurately capture such  
401 complex membranes, perhaps through combined analysis of a series of 2-D cross-sections. The

402 optimization algorithm could also successfully find the optimal structure within a few minutes,  
403 which is a great achievement compared to FIB-SEM in terms of time. Finally, the performance and  
404 properties of the reconstructed structures were consistent with the ones obtained from the original  
405 FIB-SEM structure, confirming the reliability of the presented approach.

406 With further development, a likely advantage of our approach compared to FIB-SEM is the potential  
407 to develop a 3-D reconstruction of the pore space through the entire depth of the membrane, which  
408 are typically 50–100- $\mu\text{m}$  thick. FIB-SEM analysis can only provide information on the pore space in  
409 the 1–5  $\mu\text{m}$  region at the upper surface (inlet region) of the filter, as it is experimentally impractical  
410 to mill through much more than a few microns of the membrane. In contrast, it is possible to rapidly  
411 generate cross-sectional images through the whole thickness of membranes. These images, in  
412 combination with much higher resolution images near the skin, could be used to reconstruct the pore  
413 structure throughout the entire thickness of the membrane. Such knowledge would enable  
414 fundamental investigation of the impact of the large-pore substructure on transport and mechanical  
415 properties, which have largely been neglected to-date, including in our study.

416 **References**

- 417 [1] L.-S. Wan, J.-W. Li, B.-B. Ke, Z.-K. Xu, Ordered microporous membranes templated by  
418 breath figures for size-selective separation, *J. Am. Chem. Soc.* 134 (2012) 95–98.  
419 <https://doi.org/10.1021/ja2092745>.
- 420 [2] F.A. AlMarzooqi, M.R. Bilad, B. Mansoor, H.A. Arafat, A comparative study of image  
421 analysis and porometry techniques for characterization of porous membranes, *J Mater Sci.*  
422 51 (2016) 2017–2032. <https://doi.org/10.1007/s10853-015-9512-0>.
- 423 [3] I.G. Wenten, K. Khoiruddin, A.N. Hakim, N.F. Himma, Chapter 11 - The Bubble Gas  
424 Transport Method, in: N. Hilal, A.F. Ismail, T. Matsuura, D. Oatley-Radcliffe (Eds.),  
425 *Membrane Characterization*, Elsevier, 2017: pp. 199–218. <https://doi.org/10.1016/B978-0-444-63776-5.00011-5>.
- 426 [4] W. Piątkiewicz, S. Rosiński, D. Lewińska, J. Bukowski, W. Judycki, Determination of pore  
427 size distribution in hollow fibre membranes, *Journal of Membrane Science.* 153 (1999) 91–  
428 102. [https://doi.org/10.1016/S0376-7388\(98\)00243-9](https://doi.org/10.1016/S0376-7388(98)00243-9).
- 429 [5] C. Cosentino, F. Amato, M. Ferrari, Characterization Methods for Quality Control of  
430 Nanopore and Nanochannel Membranes, in: M. Ferrari, A.P. Lee, L.J. Lee (Eds.),  
431 *BioMEMS and Biomedical Nanotechnology: Volume I Biological and Biomedical*

- 433 Nanotechnology, Springer US, Boston, MA, 2006: pp. 203–225.  
434 [https://doi.org/10.1007/978-0-387-25842-3\\_7](https://doi.org/10.1007/978-0-387-25842-3_7).
- 435 [6] H. Chamani, T. Matsuura, D. Rana, C.Q. Lan, A reverse approach to evaluate membrane  
436 pore size distribution by the bubble gas transport method using fewer experimental data  
437 points, Desalination. 518 (2021) 115287. <https://doi.org/10.1016/j.desal.2021.115287>.
- 438 [7] H. Chamani, J. Woloszyn, T. Matsuura, D. Rana, C.Q. Lan, Pore wetting in membrane  
439 distillation: A comprehensive review, Progress in Materials Science. 122 (2021) 100843.  
440 <https://doi.org/10.1016/j.pmatsci.2021.100843>.
- 441 [8] G.R. Guillen, Y. Pan, M. Li, E.M.V. Hoek, Preparation and characterization of membranes  
442 formed by nonsolvent induced phase separation: A review, Ind. Eng. Chem. Res. 50 (2011)  
443 3798–3817. <https://doi.org/10.1021/ie101928r>.
- 444 [9] L. Li, J. Wang, J. Fan, N.E. Allen, Quantification of the porosity of membranes by digital  
445 images analysis techniques, in: 2015 8th International Congress on Image and Signal  
446 Processing (CISP), 2015: pp. 984–989. <https://doi.org/10.1109/CISP.2015.7408022>.
- 447 [10] R. Ziel, A. Haus, A. Tulke, Quantification of the pore size distribution (porosity profiles) in  
448 microfiltration membranes by SEM, TEM and computer image analysis, Journal of  
449 Membrane Science. 323 (2008) 241–246. <https://doi.org/10.1016/j.memsci.2008.05.057>.
- 450 [11] M.D. Uchic, M.A. Groeber, A.D. Rollett, Automated serial sectioning methods for rapid  
451 collection of 3-D microstructure data, JOM. 63 (2011) 25–29.  
452 <https://doi.org/10.1007/s11837-011-0041-2>.
- 453 [12] M.D. Uchic, L. Holzer, B.J. Inkson, E.L. Principe, P. Munroe, Three-dimensional  
454 microstructural characterization using focused ion beam tomography, MRS Bulletin. 32  
455 (2007) 408–416. <https://doi.org/10.1557/mrs2007.64>.
- 456 [13] S.S. Manickam, J. Gelb, J.R. McCutcheon, Pore structure characterization of asymmetric  
457 membranes: Non-destructive characterization of porosity and tortuosity, Journal of  
458 Membrane Science. 454 (2014) 549–554. <https://doi.org/10.1016/j.memsci.2013.11.044>.
- 459 [14] Y. Suleiman, N. May, M. Zhang, A. Zhu, S. Zhang, J. McCutcheon, S. Shahbazmohamadi,  
460 In-situ 3D X-ray tomography and analysis of reverse osmosis membranes under  
461 compaction, Microscopy and Microanalysis. 28 (2022) 270–271.  
462 <https://doi.org/10.1017/S143192762200188X>.
- 463 [15] S.L.G. Gilleon, The influence of microstructure on membrane distillation: High-resolution  
464 3D reconstructions for analysis of pore-scale phenomena, M.S., Colorado School of Mines,  
465 2018. <https://www.proquest.com/docview/2131004079/abstract/B82B374938F24D7CPQ/1>  
466 (accessed November 1, 2022).
- 467 [16] H. Roberge, P. Moreau, E. Couallier, P. Abellan, Determination of the key structural factors  
468 affecting permeability and selectivity of PAN and PES polymeric filtration membranes  
469 using 3D FIB/SEM, Journal of Membrane Science. 653 (2022) 120530.  
470 <https://doi.org/10.1016/j.memsci.2022.120530>.
- 471 [17] M. Shirzadi, M. Ueda, K. Hada, T. Fukasawa, K. Fukui, Y. Mino, T. Tsuru, T. Ishigami,  
472 High-resolution numerical simulation of microfiltration of oil-in-water emulsion  
473 permeating through a realistic membrane microporous structure generated by focused ion  
474 beam scanning electron microscopy images, Langmuir. 38 (2022) 2094–2108.  
475 <https://doi.org/10.1021/acs.langmuir.1c03183>.
- 476 [18] G. Sundaramoorthi, M. Hadwiger, M. Ben-Romdhane, A.R. Behzad, P. Madhavan, S.P.  
477 Nunes, 3D membrane imaging and porosity visualization, Ind. Eng. Chem. Res. 55 (2016)  
478 3689–3695. <https://doi.org/10.1021/acs.iecr.6b00387>.

- 479 [19] M.M. Kłosowski, C.M. McGilvery, Y. Li, P. Abellan, Q. Ramasse, J.T. Cabral, A.G.  
480 Livingston, A.E. Porter, Micro-to nano-scale characterisation of polyamide structures of the  
481 SW30HR RO membrane using advanced electron microscopy and stain tracers, *Journal of*  
482 *Membrane Science.* 520 (2016) 465–476. <https://doi.org/10.1016/j.memsci.2016.07.063>.
- 483 [20] K.P. Brickey, A.L. Zydny, E.D. Gomez, FIB-SEM tomography reveals the nanoscale 3D  
484 morphology of virus removal filters, *Journal of Membrane Science.* 640 (2021) 119766.  
485 <https://doi.org/10.1016/j.memsci.2021.119766>.
- 486 [21] Z. Pan, Q. Ou, F.J. Romay, W. Chen, T. You, Y. Liang, J. Wang, D.Y.H. Pui, Study of  
487 structural factors of structure-resolved filter media on the particle loading performance with  
488 microscale simulation, *Separation and Purification Technology.* 304 (2023) 122317.  
489 <https://doi.org/10.1016/j.seppur.2022.122317>.
- 490 [22] C. Fager, M. Röding, A. Olsson, N. Lorén, C. von Corswant, A. Särkkä, E. Olsson,  
491 Optimization of FIB-SEM tomography and reconstruction for soft, porous, and poorly  
492 conducting materials, *Microscopy and Microanalysis.* 26 (2020) 837–845.  
493 <https://doi.org/10.1017/S1431927620001592>.
- 494 [23] T. Prill, C. Redenbach, D. Roldan, M. Godehardt, K. Schladitz, S. Höhn, K. Sempf,  
495 Simulating permeabilities based on 3D image data of a layered nano-porous membrane,  
496 *International Journal of Solids and Structures.* 184 (2020) 3–13.  
497 <https://doi.org/10.1016/j.ijsolstr.2019.04.010>.
- 498 [24] P. Diblíková, M. Veselý, P. Sysel, P. Čapek, Reconstructing the microstructure of  
499 polyimide–silicalite mixed-matrix membranes and their particle connectivity using FIB-  
500 SEM tomography, *Journal of Microscopy.* 269 (2018) 230–246.  
501 <https://doi.org/10.1111/jmi.12618>.
- 502 [25] A. Nanjundappa, A.S. Alavijeh, M. El Hannach, D. Harvey, E. Kjeang, A customized  
503 framework for 3-D morphological characterization of microporous layers, *Electrochimica*  
504 *Acta.* 110 (2013) 349–357. <https://doi.org/10.1016/j.electacta.2013.04.103>.
- 505 [26] H. Ostadi, P. Rama, Y. Liu, R. Chen, X.X. Zhang, K. Jiang, 3D reconstruction of a gas  
506 diffusion layer and a microporous layer, *Journal of Membrane Science.* 351 (2010) 69–74.  
507 <https://doi.org/10.1016/j.memsci.2010.01.031>.
- 508 [27] M.S. Riasi, L. Tsaur, Y.M. Li, Q. Zhang, U. Wiesner, L. Yeghiazarian, Stochastic  
509 microstructure delineation and flow simulation in asymmetric block copolymer  
510 ultrafiltration membranes, *Journal of Membrane Science.* 668 (2023) 121163.  
511 <https://doi.org/10.1016/j.memsci.2022.121163>.
- 512 [28] A.-M. Simundic, Confidence interval, *Biochem Med.* 18 (2008) 154–161.  
513 <https://doi.org/10.11613/BM.2008.015>.
- 514 [29] R. Daneshjou, K. Vodrahalli, R.A. Novoa, M. Jenkins, W. Liang, V. Rotemberg, J. Ko,  
515 S.M. Swetter, E.E. Bailey, O. Gevaert, P. Mukherjee, M. Phung, K. Yekrang, B. Fong, R.  
516 Sahasrabudhe, J.A.C. Allerup, U. Okata-Karigane, J. Zou, A.S. Chiou, Disparities in  
517 dermatology AI performance on a diverse, curated clinical image set, *Science Advances.* 8  
518 (2022) eabq6147. <https://doi.org/10.1126/sciadv.abq6147>.
- 519 [30] M.A. Thornton, D.I. Tamir, People accurately predict the transition probabilities between  
520 actions, *Science Advances.* 7 (2021) eabd4995. <https://doi.org/10.1126/sciadv.abd4995>.
- 521 [31] H. Nazem-Bokaee, F. Fallahianbijan, D. Chen, S.M. O'Donnell, C. Carrello, S. Giglia, D.  
522 Bell, A.L. Zydny, Probing pore structure of virus filters using scanning electron  
523 microscopy with gold nanoparticles, *Journal of Membrane Science.* 552 (2018) 144–152.  
524 <https://doi.org/10.1016/j.memsci.2018.01.069>.

- 525 [32] P. Kosiol, M.T. Müller, B. Schneider, B. Hansmann, V. Thom, M. Ulbricht, Determination  
526 of pore size gradients of virus filtration membranes using gold nanoparticles and their  
527 relation to fouling with protein containing feed streams, *Journal of Membrane Science*. 548  
528 (2018) 598–608. <https://doi.org/10.1016/j.memsci.2017.11.048>.
- 529 [33] K.K. Singh, A. Singh, A study of image segmentation algorithms for different types of  
530 images, *Int. J. Comput. Sci.* 7 (2010) 414–417.
- 531 [34] A. Janwale, Plant leaves image segmentation techniques: A review, *Int. J. Comput. Sci.  
532 Eng.* 5 (2017) 147–150.
- 533 [35] P. Roy, S. Dutta, N. Dey, G. Dey, S. Chakraborty, R. Ray, Adaptive thresholding: A  
534 comparative study, in: 2014 International Conference on Control, Instrumentation,  
535 Communication and Computational Technologies (ICCICCT), 2014: pp. 1182–1186.  
536 <https://doi.org/10.1109/ICCICCT.2014.6993140>.
- 537 [36] D. Bradley, G. Roth, Adaptive thresholding using the integral image, *Journal of Graphics  
538 Tools*. 12 (2007) 13–21. <https://doi.org/10.1080/2151237X.2007.10129236>.
- 539 [37] D. Tian, A review on image feature extraction and representation techniques, *Int. J.  
540 Multimedia Ubiquitous Eng.* 8 (2013) 385–395.
- 541 [38] A. Rabbani, M. Babaei, Hybrid pore-network and lattice-Boltzmann permeability  
542 modelling accelerated by machine learning, *Advances in Water Resources*. 126 (2019)  
543 116–128. <https://doi.org/10.1016/j.advwatres.2019.02.012>.
- 544 [39] A.P. Generale, S.R. Kalidindi, Reduced-order models for microstructure-sensitive effective  
545 thermal conductivity of woven ceramic matrix composites with residual porosity,  
546 *Composite Structures*. 274 (2021) 114399.  
547 <https://doi.org/10.1016/j.compstruct.2021.114399>.
- 548 [40] Z. Hadjadj, M. Cheriet, A. Meziane, Y. Cherfa, A new efficient binarization method:  
549 application to degraded historical document images, *SIViP*. 11 (2017) 1155–1162.  
550 <https://doi.org/10.1007/s11760-017-1070-2>.
- 551 [41] N. Bhargava, A. Kumawat, R. Bhargava, Fingerprint matching of normalized image based  
552 on Euclidean distance, *Int. J. Comput. Appl.* 120 (2015) 20–23.
- 553 [42] T. Opacic, S. Dencks, B. Theek, M. Piepenbrock, D. Ackermann, A. Rix, T. Lammers, E.  
554 Stickeler, S. Delorme, G. Schmitz, F. Kiessling, Motion model ultrasound localization  
555 microscopy for preclinical and clinical multiparametric tumor characterization, *Nat  
556 Commun.* 9 (2018) 1527. <https://doi.org/10.1038/s41467-018-03973-8>.
- 557 [43] R. Mukherjee, F. Sauvage, H. Xie, R. Löw, F. Mintert, Preparation of ordered states in  
558 ultra-cold gases using Bayesian optimization, *New J. Phys.* 22 (2020) 075001.  
559 <https://doi.org/10.1088/1367-2630/ab8677>.
- 560 [44] R. Martinez-Cantin, BayesOpt: A Bayesian optimization library for nonlinear optimization,  
561 experimental design and bandits, *Journal of Machine Learning Research*. 15 (2014) 3915–  
562 3919.
- 563 [45] P. Agrawal, A. Mascini, T. Bultreys, H. Aslannejad, M. Wolthers, V. Cnudde, I.B. Butler,  
564 A. Raoof, The impact of pore-throat shape evolution during dissolution on carbonate rock  
565 permeability: Pore network modeling and experiments, *Advances in Water Resources*. 155  
566 (2021) 103991. <https://doi.org/10.1016/j.advwatres.2021.103991>.
- 567 [46] E.C. Rooney, V.L. Bailey, K.F. Patel, M. Dragila, A.K. Battu, A.C. Buchko, A.C. Gallo, J.  
568 Hatten, A.R. Possinger, O. Qafoku, Loren.R. Reno, M. SanClements, T. Varga, R.A.  
569 Lybrand, Soil pore network response to freeze-thaw cycles in permafrost aggregates,  
570 *Geoderma*. 411 (2022) 115674. <https://doi.org/10.1016/j.geoderma.2021.115674>.

- 571 [47] Z.K. Akasheva, D.A. Bolysbek, B.K. Assilbekov, A.K. Yergesh, A.Y. Zhanseit, Pore-  
572 network modeling and determination of rock and two-phase fluid flow properties,  
573 Engineering Journal of Satbayev University. 143 (2021) 106–114.  
574 <https://doi.org/10.51301/vest.su.2021.i3.15>.
- 575 [48] J. Meng, S. Zhang, Z. Cao, C. Wang, Pore structure characterization based on the panxi  
576 coal molecular model, Natural Resources Research. 31 (2022) 2731–2747.
- 577 [49] A. Guo, W.C. Marshall, C.C. Woodcock, J.L. Plawsky, Transport in mazes; simple  
578 geometric representations to guide the design of engineered systems, Chemical Engineering  
579 Science. 250 (2022) 117416. <https://doi.org/10.1016/j.ces.2021.117416>.
- 580 [50] Q. Xiong, T.G. Baychev, A.P. Jivkov, Review of pore network modelling of porous media:  
581 Experimental characterisations, network constructions and applications to reactive  
582 transport, Journal of Contaminant Hydrology. 192 (2016) 101–117.  
583 <https://doi.org/10.1016/j.jconhyd.2016.07.002>.
- 584 [51] Y. Song, E. Shim, 3D X-ray tomographic microstructure analysis of dust-clogging inside  
585 nonwoven fibrous filter media, Journal of Membrane Science. 664 (2022) 121067.  
586 <https://doi.org/10.1016/j.memsci.2022.121067>.
- 587 [52] K.P. Russell, A.L. Zydny, E.D. Gomez, Impact of virus filter pore size / morphology on  
588 virus retention behavior, Journal of Membrane Science. 670 (2023) 121335.  
589 <https://doi.org/10.1016/j.memsci.2022.121335>.

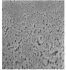
591

## 592 Acknowledgments

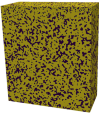
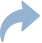
593 This work was supported by the Acceleration Consortium at the University of Toronto. Funding for  
594 this work was also provided by the Natural Sciences and Engineering Research Council of Canada  
595 (Alliance Grant ALLRP 570714-2021). KR, AZ, and EG acknowledge support from the Membrane  
596 Science, Engineering, and Technology (MAST) Center, which is funded by grant number 1841474  
597 from the U.S. NSF IUCRC program.

598 **Data and materials availability:** The code is available on GitHub Repository: Hooman-  
599 Chamani/3DReconstruction: Membrane Microstructure Project ([github.com](https://github.com)). The FIB-SEM data set  
600 of the virus filter is also present in the paper Supplementary Materials.

# Image Segmentation Feature Extraction Optimization

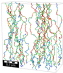
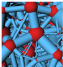


2-D SEM image



3-D structure

Performance  
and Properties



Flux  
Pore Network  
Model